

AGAPEROS: Searches for microlensing in the LMC with the Pixel Method

I. Data treatment and pixel light curves production

A.-L. Melchior^{1,2,3}, C. Afonso⁴, R. Ansari⁵, É. Aubourg⁴, P. Baillon⁶, P. Bareyre⁴, F. Bauer⁴, J.-Ph. Beaulieu⁷, A. Bouquet², S. Brehin⁴, F. Cavalier⁵, S. Char⁸, F. Couchot⁵, C. Coutures⁴, R. Ferlet⁷, J. Fernandez⁸, C. Gauchere¹⁴, Y. Giraud-Héraud², J.-F. Glicenstein⁴, B. Goldman⁴, P. Gondolo^{2,9}, M. Gros⁴, J. Guibert¹⁰, C. Gry¹¹, D. Hardin⁴, J. Kaplan², J. de Kat⁴, M. Lachièze-Rey⁴, B. Laurent⁴, É. Lesquoy⁴, Ch. Magneville⁴, B. Mansoux⁵, J.-B. Marquette⁷, E. Maurice¹², A. Milsztajn⁴, M. Moniez⁵, O. Moreau¹⁰, L. Moscoso⁴, N. Palanque-Delabrouille⁴, O. Perdereau⁵, L. Prévôt¹², C. Renault⁴, F. Queinnec⁴, J. Rich⁴, M. Spiro⁴, A. Vidal-Madjar⁷, L. Vigroux⁴, S. Zylberajch⁴

¹ Astronomy Unit, Queen Mary and Westfield College, Mile End Road, London E1 4NS, UK

² Laboratoire de Physique Corpusculaire et Cosmologie (UMR 7535), Collège de France, 75231 Paris Cedex 05, France

³ NASA/Fermilab Astrophysics Center, Fermi National Accelerator Laboratory, Batavia, IL 60510-0500, USA

⁴ CEA, DSM, DAPNIA, Centre d'Études de Saclay, 911191 Gif-sur-Yvette Cedex, France

⁵ Laboratoire de l'Accélérateur Linéaire, IN2P3 CNRS, Université Paris-Sud, 91405 Orsay Cedex, France

⁶ CERN, 1211 Genève 23, Switzerland

⁷ Institut d'Astrophysique de Paris, CNRS, 98 bis Boulevard Arago, 75014 Paris, France

⁸ Universidad de la Serena, Facultad de Ciencias, Departamento de Fisica, Casilla 554, La Serena, Chile.

⁹ Max-Planck-Institut für Physik, Föhringer Ring 6, 80805 München, Germany

¹⁰ Centre d'Analyse des Images de l'INSU, Observatoire de Paris, 61 avenue de l'Observatoire, 75014 Paris, France

¹¹ Laboratoire d'Astronomie Spatiale de Marseille, Traverse du Siphon, Les Trois Lucs, 13120 Marseille, France

¹² Observatoire de Marseille, 2 place Le Verrier, 13248 Marseille Cedex 04, France

Received / Accepted

Abstract. The presence and abundance of MAssive Compact Halo Objects (MACHOs) towards the Large Magellanic Cloud (LMC) can be studied with microlensing searches. The 10 events detected by the EROS and MACHO groups suggest that objects with $0.5M_{\odot}$ could fill 50% of the dark halo. This preferred mass is quite surprising, and increasing the presently small statistics is a crucial issue. Additional microlensing of stars too dim to be resolved in crowded fields should be detectable using the Pixel Method. We present here an application of this method to the EROS 91-92 data (one tenth of the whole existing data set). We emphasize the data treatment required for monitoring pixel fluxes. Geometric and photometric alignments are performed on each image. Seeing correction and error estimates are discussed. $3.6'' \times 3.6''$ super-pixel light curves, thus produced, are very stable over the 120 days time-span. Fluctuations at a level of 1.8% of the flux in blue and 1.3% in red are measured on the pixel light curves. This level of stability is comparable with previous estimates. The data analysis dedicated to the search of possible microlensing events together with

refined simulations will be presented in a companion paper.

Key words: Methods: data analysis – Techniques: photometric – Galaxy: halo – Galaxies: Magellanic Clouds – Cosmology: dark matter – Cosmology: gravitational lensing

1. Introduction

The amount and nature of Dark Matter present in the Universe is an important question for cosmology (see White et al. (1996) for current status). At the galaxies scale (Ashman 1992), dynamical studies (Zaritsky 1992) as well as macrolensing analysis (Carollo et al. 1995) show that up to 90 % of the galactic masses might not be visible. One plausible scheme is that the stellar content of galaxies is embedded in a dark halo. Primordial nucleosynthesis (Walker et al. 1991; Copi et al. 1995) predicts a larger number of baryons than what is seen (Persic & Salucci 1992). Dark baryons hidden in gaseous or compact objects (Carr 1994, Gerhard & Silk 1996) could explain the dark galactic halos.

In 1986, Paczynski proposed microlensing techniques for measuring the abundance of compact objects in galactic halos. The LMC stars are favourable targets for microlensing events searches. Since 1990 and 1992, the EROS (Aubourg et al. 1993) and MACHO (Alcock et al. 1993) groups have studied this line of sight. The detection of 10 microlensing events has been claimed in the large mass range $0.05 - 1 M_{\odot}$ (Aubourg et al. 1993, Alcock et al. 1996). This detection rate, smaller than expected with a full halo, indicates that the most likely fraction of compact objects in the dark halo is $f = 0.5$ (Alcock et al. 1996). Moreover the most probable mass for the lens is $0.5^{+0.3}_{-0.2} M_{\odot}$ which remains unexplained (see for instance Gould 1996a, Kerins 1997). In parallel, the small mass range ($5 \times 10^{-7} M_{\odot} < M < 2 \times 10^{-3} M_{\odot}$) has been excluded by the EROS group, with CCD data of the LMC bar as described in various publications (Queinnec 1994, Aubourg et al. 1995, Renault 1996). Such small mass objects could not account for more than 20% of the standard halo mass. In the meantime, the DUO (Alard 1995), MACHO (Alcock et al. 1995) and OGLE (Udalski 1995) groups look towards the galactic bulge where star-star events are expected. The detection rate is higher than expected with galactic models (see for instance Evans 1994, Alcock et al. 1995, Stanek et al. 1997). The events detected in these two directions demonstrate the efficacy of the microlensing techniques based on the monitoring of several millions of stars.

Microlensing Searches with the Pixel Method The detection of a larger number of events is one of the big challenges in microlensing searches. This basically requires the monitoring of a larger number of stars. The Pixel Method, initially presented by Baillon et al. (1993), gives a new answer to this problem: monitoring pixel fluxes. On galaxy images, most of the pixel fluxes comes from unresolved stars, which contribute to the background flux. If the flux of one of these stars is microlensed, the pixel flux will be amplified. Such a luminosity variation can be detected above a given threshold, provided the amplification is large enough. This pixel monitoring approach has two types of application. First, it allows to investigate towards more distant galaxies and thus to study some other lines of sight. Secondly, it can be applied on existing data extending the sensitivity of previous analysis to unresolved stars.

The former point has given rise to observations of the M31 galaxy. The AGAPE team (Ansari et al. 1997) has shown that this method works on M31 data. Luminosity variations compatible with the expected microlensing events have been detected but the complete analysis is still in progress (Giraud-Héraud 1997). A similar approach, though technically different, called Differential Image Photometry is also investigated by the VATT/Columbia collaboration (Crotts 1992, Tomaney & Crotts 1996). Some prospective work has also been done towards M87 (Gould

1995). A theoretical study of the so-called pixel lensing has been published by Gould (1996b). The implementation of the Pixel Method on part of the CCD data (91-94) collected by the EROS collaboration in the direction of the LMC is the subject of this paper (Paper I).

Because of the relatively small number of resolved stars on the images, the star monitoring analysis (Queinnec 1994, Aubourg et al. 1995, Renault 1996) applied on these data was mainly able to detect events due to low mass compact objects. On the EROS LMC images, a large fraction of the stars remains unresolved: typically 5 to 10 stars contribute to 95% of the pixel flux in one square arcsecond. Our analysis of the same data using pixel monitoring allows to increase the sensitivity of microlensing searches and to extend the mass range of interest up to $0.5 M_{\odot}$, as will be shown in Paper II (Melchior et al., in preparation). In this paper, we focus on the data treatment, required for the construction of pixel light curves, and we discuss the stability achieved.

In Sect. 2, we start with a short description of the data used. In Sect. 3, we successively describe the geometric and photometric alignments applied on the images. We are thus able to build pixel light curves and to discuss their stability achieved after this preliminary treatment. In Sect. 4, we average the images of each night, improving the stability considerably. In Sect. 5, we correct the seeing variations and obtain optimal light curves cleaned from most variations of the observational conditions. In order to account for spurious effects present on the light curves, in Sect. 6, we estimate error estimates for each pixel flux. In Sect. 7, we conclude that this complete treatment provides pixel light curves with a level of noise compatible with expectations discussed in Baillon et al (1993). We will describe the analysis of the data and the filtering of possible microlensing events in Paper II.

2. The data

2.1. Description of the data set

These data have been collected at La Silla ESO observatory in Chile with a 40cm telescope ($f/10$) equipped with a thick CCD camera composed of 8×2 CCD chips of 400×579 pixels with scale of $1.21''/\text{pixel}$ (Arnaud et al., 1994b, Queinnec, 1994 and Aubourg et al., 1995). The gain of the camera was $6.8e^-/\text{ADU}$ with a read-out noise of 12 photo-electrons. For the 1991-92 campaign only 11 chips out of 16 were active. Due to technical problems, we only analyse 10. The monitoring has been performed in two wide color bands (Arnaud et al., 1994a). Exposure times were set to 8 min in red ($\langle \lambda \rangle = 670 \text{ nm}$) and 15 min in blue ($\langle \lambda \rangle = 490 \text{ nm}$). As the initial goal was to study microlensing events with a short-time scale (Aubourg et al. 1995), up to 20 images per night in both color are available. A total of 2000 blue and red images were collected during 95 nights spread over a 120 days period (18 December 1991 - 11 April 1992). The combined CCD and filter

efficiency curves as shown in Grison et al. (1994) lie below 15% in blue and below 35% in red. Bias subtraction and flat-field has been performed on-line by the EROS group.

The seeing varies between 1.3 and 3 arcsecond with a mean value of 2.4 arcsecond (typical dispersion 0.4 arcsecond). It should be emphasized that the observational strategy (exposure time) had been optimized for star monitoring. In other words, this means that the photon noise associated with the mean flux (typically 280 ADU per pixel in red and 100 ADU in blue) is relatively large: 6.6 ADU in red and 3.8 ADU in blue. To apply the Pixel Method to this data set, we take advantage of the large number of images available each night, increasing the signal-to-noise ratio with an averaging procedure.

2.2. Absolute calibration

The treatment described below is performed with respect to a reference image. The correspondence between the flux measured on these images and the magnitude, deduced from Grison et al (1995), is as follows:

$$m_B = -2.5 \log \phi_B + 24.8 \quad (1)$$

$$m_R = -2.5 \log \phi_R + 24.9 \quad (2)$$

Note that the constant of magnitude is about the same in the two colors, whereas the background flux is much larger in red than in blue. The correspondence with the Johnson-Cousins system can be found in Grison et al. (1995).

The aim of the whole treatment presented in the following is to obtain pixel light curves properly corrected for variations of the observational conditions. The PEIDA package used by the EROS group was adapted for pixel monitoring. This treatment is applied to the first CCD campaign (1991-92) of the EROS group on the LMC bar, i.e. 10% of the whole data set analysed in Renault (1996).

3. Image alignments

The alignments described in this section are needed in order to be able to build pixel light curves from images that are never taken in the same observing conditions. Firstly, the telescope never points twice exactly in the same direction and the geometric alignment insures that the same area of the LMC contributes to the same pixel flux, through the whole period of observation. Secondly, photometric conditions, atmospheric absorption and sky background light, change from one frame to the other. The photometric alignment corrects for these global variations.

Errors affecting pixel fluxes after these corrections are a key issue as discussed through this section. It is not obvious how to disentangle the various sources of error introduced at each step, and global errors, including *all* sources of noise, will be computed for each pixel flux in Sect. 6.

3.1. Geometric alignment

Between exposures, images are shifted by as much as 40 pixels and this displacement has to be corrected, in order to insure that each pixel always covers the same area of the LMC. As emphasized below, errors still affect the pixel flux after this alignment and two components can be distinguished. The first one, resulting from the uncertainty in the parameters of displacement, turns out to be negligible, whereas the second one, introduced by the linear interpolation, is an important source of noise. In this section, we give a qualitative overview of these sources of errors. This study, based on synthetic images, allows to disentangle errors due to the geometrical alignment from other effects present on real images because the position and content of unaligned frames are known by construction.

Parameter of displacement The parameters of displacement are determined with the PEIDA algorithm (see Ansari, 1994), based on the matching of stars positions. Beside translation, rotation and dilatation are also taken into account as far as their amplitude remains small (otherwise the corresponding images are removed from further considerations).

A series of mock images synthetized with the parameters of real images (geometric displacement, absorption, sky background and seeing) allow to estimate the mean error on the pixel position to be 0.011 ± 0.005 pixel. Similar estimates have been obtained by the EROS group (Reza Ansari, private communication) on real data.

This introduces a quite small mismatch on pixel fluxes: in first approximation, the error on the flux is proportional to the pixel area corresponding to the difference between the true and the computed pixel position.

Linear interpolation Once the parameters of displacement are estimated, pixel fluxes are corrected with a linear interpolation. This interpolation is necessary in order to monitor pixel fluxes, and to build pixel light curves. We use synthetic images to understand qualitatively the residual errors. Two sets of blue images are simulated with the identical fluxes (new moon condition) and seeings (2.5 arcsecond) but shifted in both directions with respect to one of them (the “reference” image). A linear interpolation is applied to each of these images in order to match the position of the reference. In case of pure translation, the corrected flux is computed with the flux of the 4 pixels overlapping the pixel p on the reference frame: the areas of these intersections with this pixel p are used to weight each pixel flux. The square of the variable v , depending upon δx and δy , the displacement in the x and y directions:

$$v = \sqrt{(\delta x^2 + (1 - \delta x)^2) (\delta y^2 + (1 - \delta y)^2)} \quad (3)$$

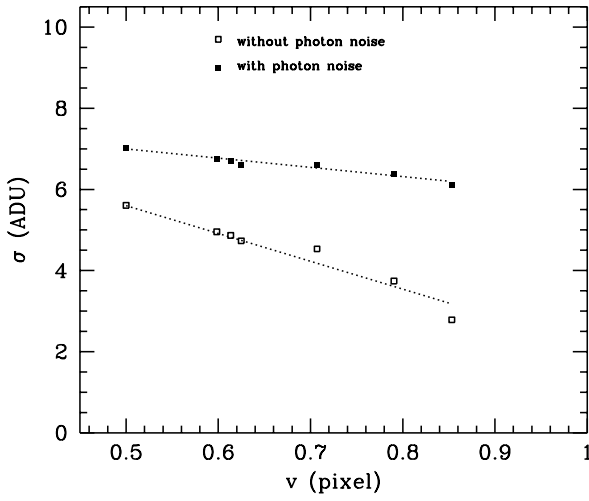


Fig. 1. Error due to linear interpolation estimated with two sets of synthetic images: σ is the dispersion measured on the flux difference between pixels on the “reference” image and corrected images; the x-axis shows the variable v , a function of the displacement discussed in the text.

is the sum of the square of these overlapping surfaces. It characterizes the mixing of pixel fluxes produced by this interpolation: the smaller is v , the more pixels are mixed by the interpolation.

Figure 1 displays an estimate of the residual errors affecting pixel fluxes for different displacement parameters, and shows a correlation of the errors with the variable v . The first set of images, simulated without photon noise, shows errors on pixel fluxes due to linear interpolation smaller than 5.5 ADU (about 4.5% of the mean flux). The second set of images, simulated with photon noise, allows to check that the photon noise adds quadratically with the “interpolation” noise and residual errors are smaller than 7 ADU. The correlation observed on this figure between the error σ and the variable v can be understood as follows: when v decreases, the interpolated image gets more and more degraded, and the interpolation noise increases while the poisson noise is smeared out.

This residual error is strongly seeing dependent. If the same operation as above is performed, but on an image, with a seeing of 2 arcsecond, residual errors are as large as 10% of the mean flux: the larger the seeing difference, the larger the residual error. As the seeing of raw images varies between 1.3 and 3 arcsecond, this makes a detailed error tracing very difficult. In Sect. 6, we evaluate the errors in a global way.

An important consequence of the linear interpolation is that the seeing is degraded. Figure 2 shows the distri-

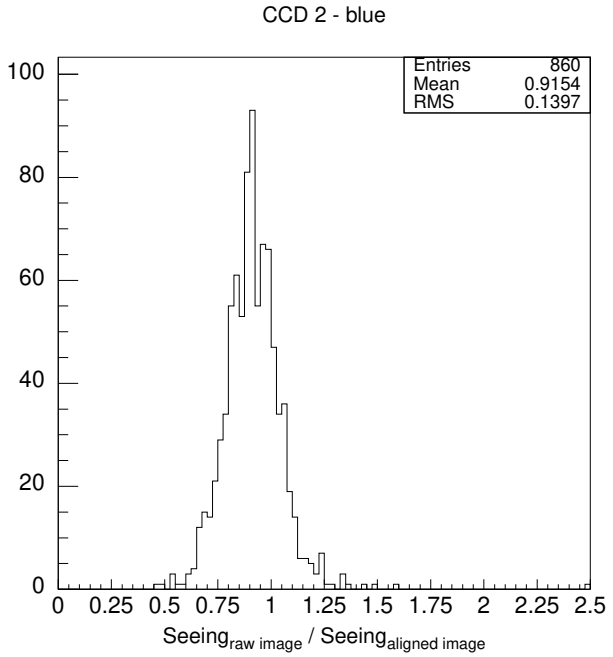


Fig. 2. Ratio of the mean seeing measured on each image before and after the geometric alignment.

bution of the ratio between the seeing values measured on raw and aligned real images. After linear interpolation, the PSF on each image is around 10% larger than before. But more importantly, its shape is altered: widened in the direction of the displacement.

As will be explained with further details in Sect. 4, the images used in the subsequent analysis are averaged images therefore affected by reduced noise.

3.2. Photometric alignment

Changes in observational conditions (atmospheric absorption and background flux) are taken into account with a global correction relative to the reference image. We assume that a linear correction is sufficient:

$$\phi_{\text{corrected}} = a\phi_{\text{raw}} + b \quad (4)$$

where $\phi_{\text{corrected}}$ and ϕ_{raw} are the pixel fluxes after and before correction respectively. The absorption factor a is estimated for each image with a PEIDA procedure based on the comparison of star flux (Ansari, 1994). Sky background excess is supposed to affect pixel fluxes by an additional term b which differs from one image to another.

In Fig. 3, we plot the absorption factor (top) and the sky background (bottom) estimated for each image with respect to the reference image as a function of time. The absorption varies by a factor 2 within the same night. During the full moon periods, the background flux can be up to 20 times higher than during moonless nights, increasing the statistical fluctuations by a factor up to 4.5. However, such a level of noise concerns very few images (see Fig.

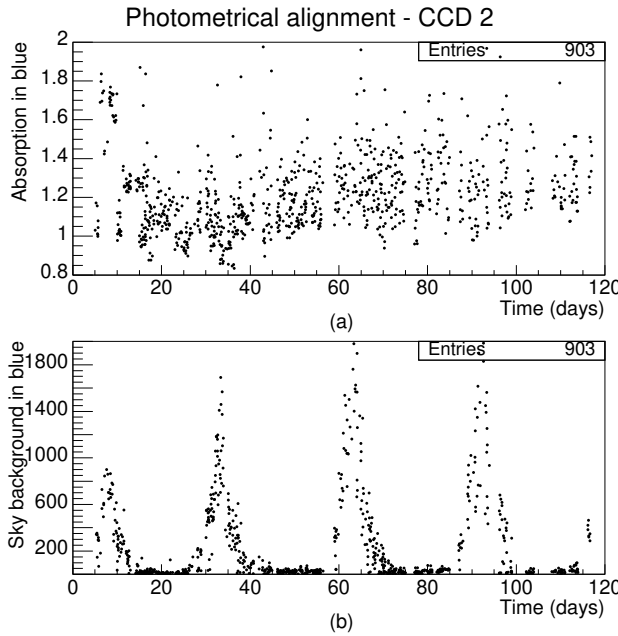


Fig. 3. Absorption (a) and sky background (b) estimated for each blue image

3), and only about 20% of the images more than double their statistical fluctuations. Despite their large noise, full moon images improve the temporal sampling, and at the end of the whole treatment, the error bars associated with these points are not significantly larger than the ones corresponding to new moon periods, except for a few nights.

At this stage, it is not obvious how to disentangle the error due to the photometric alignment from other sources of error and noise. We expect large errors for images with strong systematic effects, such as, for instance, non homogeneous PSF. These errors will be included in global error estimates described in Sect. 6.

3.3. Correction of residual large scale variations

We note the presence of a variable spatial pattern particularly important during full moon periods. This residual effect, probably due to reflected light, can be eliminated with a procedure similar to the one applied on the AGAPE data, as described in Ansari et al. (1997). We calculate a median image with a grid of 9×9 pixels on the difference between each studied image and the reference image. It is important to work on the difference in order to eliminate the disturbing contribution of stars which perturbs the calculation of the median. Then we subtract the corresponding median from each image, we thus filter out large scale spatial variations. In Fig. 4, we show a light curve for which the full treatment with and without this correction is applied. Above, the pixel light curve presents important systematic effects during full moon periods, whereas,

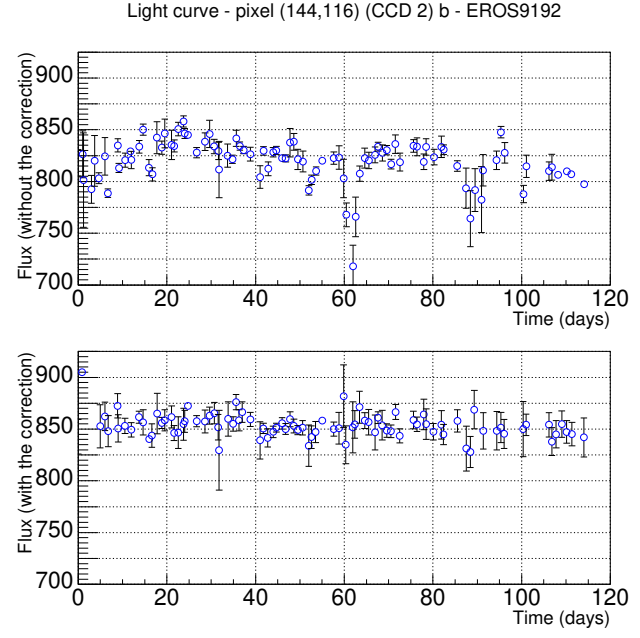


Fig. 4. Pixel light curve without (above) and with (below) filtering out of large scale spatial variations.

below, the systematic effects have disappeared after correcting for these large scale variations.

3.4. Image selection

After these alignments, we eliminate images with parameters lying in extreme ranges. We keep images, with no obvious defects, in the following parameter range in both color:

- Absorption factor:
 $0.6 < a^R < 1.5 ; 0.6 < a^B < 1.5$
- Mean flux (ADU):
 $100.0 < \langle \phi^R \rangle < 2000.0$
 $70.0 < \langle \phi^B \rangle < 1500.0$
- Seeing (arcsec):
 $S^R < 3.0 ; S^B < 3.0$

The whole procedure rejects about 33 % of the data, thus reducing the number of images used.

3.5. Stability of elementary pixels after alignment

We are now able to build pixel light curves, made of around 1000 measurements spread over 120 days. The stability can be expressed in term of the relative dispersion $\sigma/\langle \phi \rangle$ measured for each light curve, where $\langle \phi \rangle$ stands for the mean flux on the light curve and σ is the dispersion along the light curve. This dispersion gives us a global estimate of the errors introduced by the alignments, combined with all other sources of noise (photon noise, readout noise...). In Fig. 5, we present the histogram of this

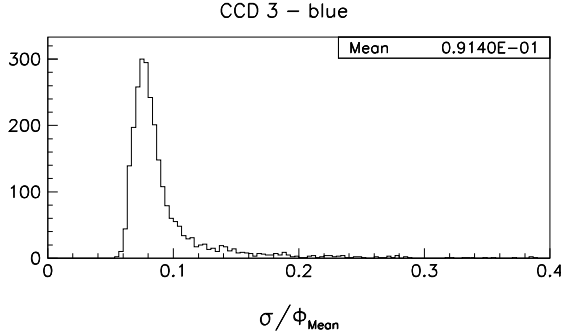


Fig. 5. Stability obtained in blue with 1000 *pixel* flux measurements spread over 120 days, which covers a 50×50 patch of CCD 3.

dispersion for one 50×50 patch of one CCD field, which shows a mean dispersion of 9.1%. This dispersion includes all sources of noise present on the images, in particular those discussed above (in Sect. 3.1,3.2), which seem to account for the bulk of the fluctuations. With such a noise level, dominated at this stage by photon counting and flux interpolation errors, one does not expect a good sensitivity to luminosity variations. Fortunately, various improvements can still reduce this dispersion by a factor of 4, and are described in the following.

4. Going to one image per night

The motivation of this pixel analysis is to increase the sensitivity for long duration events (≥ 5 days) in the mass range where all the known candidates have been observed. It is crucial to note that a time-sampling of 1 measurement per day is sufficient. Adding the numerous images available each night (up to 20 per night) allow to reduce the level of noise discussed in Sect. 3.5.

4.1. Construction

We average the images of each night. During the night n , we have N_n^p measurements j of pixel p flux $\phi_{n,j}^p$ ($j = 1, N_n^p$). The typical number of measurements N_n^p available each night is shown in Fig. 6. Between 1 and 20 images with an average of 10 images are available each night. As emphasized in Sect. 6, this is moreover very useful for the error estimation. The mean flux ϕ_n^p of this pixel over the night is computed removing¹ the fluxes which deviate more than 3σ from the mean:

$$\phi_n^p = \frac{1}{N_n^p} \sum_{j=1}^{N_n^p} \phi_{n,j}^p \quad (5)$$

This procedure is a crucial step as it reduces the large dispersion mentioned above. This 3σ cut-off removes any

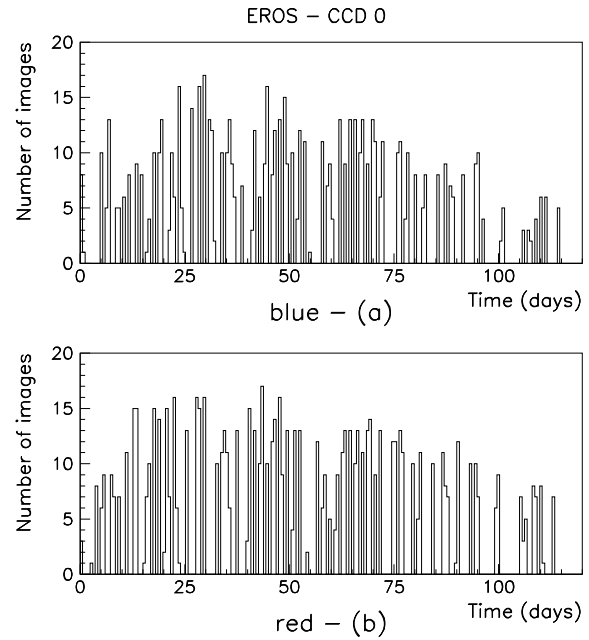


Fig. 6. Number of images per night for one CCD field: in red (a) and in blue (b)

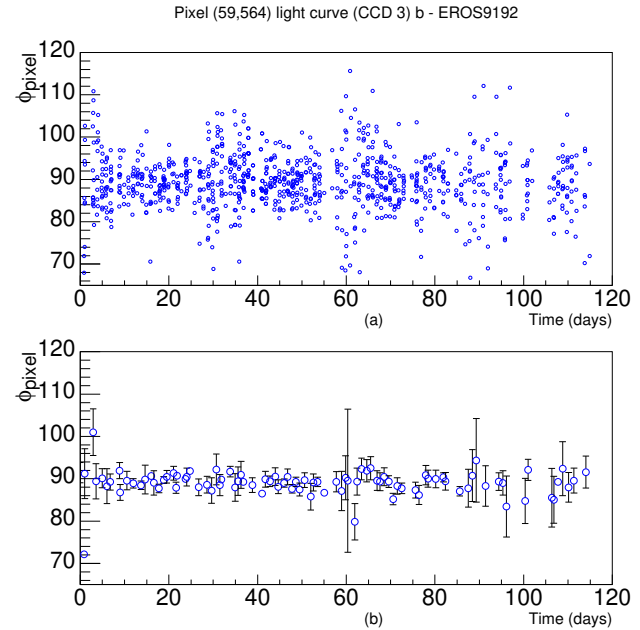


Fig. 7. Stable pixel light curve (a) before and (b) after the mean is performed over each night

large fluctuation due to cosmic rays, as well as CCD defects and border effects. Figure 7 shows the result of this operation on one pixel light curve. The dispersion which affects the measures on the top panel (a) is reduced and included in the error bars associated to each mean pixel flux as show on the bottom panel (b) (see Sect. 6 for more

¹ Note that, due to this cut-off, the number of measurements N_n^p used for a given night can differ from pixel to pixel.

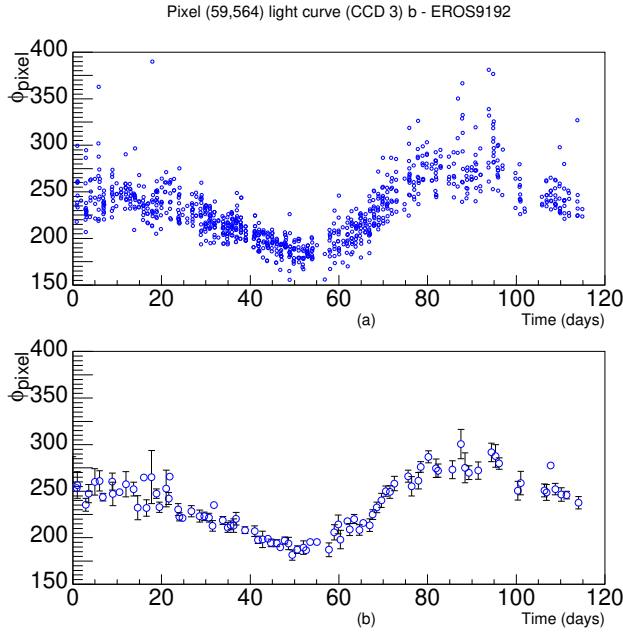


Fig. 8. Variable pixel light curve before (a) and after (b) the mean is performed over each night

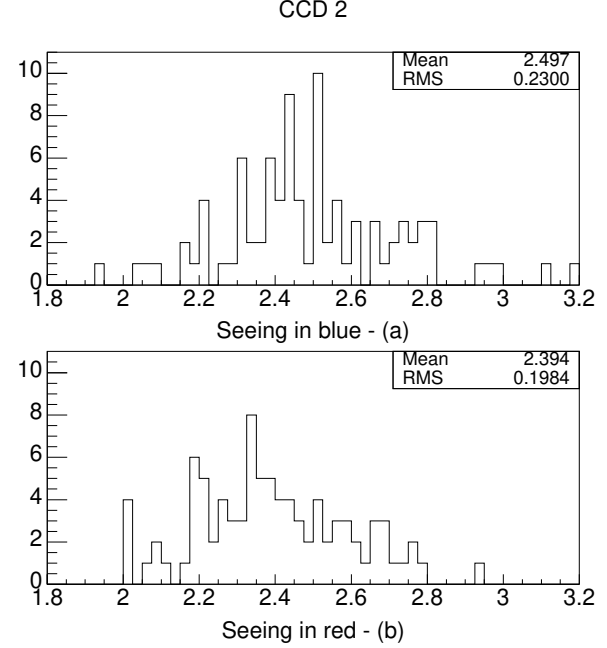


Fig. 10. Histogram of seeing on mean images

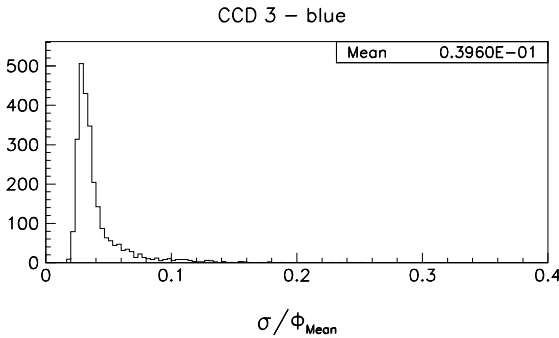


Fig. 9. Stability achieved on pixel light curves after averaging the images of each night, on a 50×50 patch of CCD 3.

details about the computation of these error bars). Figure 8 shows the same operation applied on a pixel light curve exhibiting a long time scale variation. One can notice that error bars associated to measurements performed during full moon periods are not systematically larger than those corresponding to new moon periods. This confirms the fact that errors are not dominated by photon noise anymore. Figure 9 displays the histogram of relative stability for the resulting light curves, for the same area as for Fig. 5. A mean dispersion of 3.9% is measured: the noise is thus reduced by a factor 2.

To summarize, this procedure improves the image quality, reduces the fluctuations mentioned above and removes cosmic rays. In particular, the seeing on these composite images becomes more homogeneous with an average

value of 2.5 arcsecond in red and 2.4 arcsecond in blue and a quite small dispersion of 0.2 arcsecond, as displayed in Fig. 10. The seeing dispersion is divided by a factor 2 with respect to initial individual images, whereas the average value is similar.

4.2. Light curves and stability

A significant improvement can still be done by considering super-pixel light curves. Super-pixels are constructed with a running window of 3×3 pixels, keeping thus as many super-pixel light curves as we have pixels. These $3.6'' \times 3.6''$ super-pixels are taken large enough to encompass most of the flux of a centered star, but not too large in order to avoid surrounding contaminants and dilution of the signal. As such, they are an optimum for this dense star field given the seeing conditions. As shown in Fig. 11 for the whole CCD 3, a relative dispersion of the superpixel flux is measured at a level of 2.1% in blue and 1.6% in red.

5. Seeing correction

Beside the good stability discussed above, fluctuations of the super-pixel fluxes due to seeing variations are still present. For a star lying in the central pixel (of the 3×3 patch), on average 80% of the star flux enters the superpixel for a gaussian PSF², but this seeing fraction varies with the seeing. The treatment of these residual variations is a crucial point for pixel monitoring. As described in the remainder of this section, we are able to correct them for

² Note that for real PSF, tails are expected to be larger than those of a gaussian PSF.

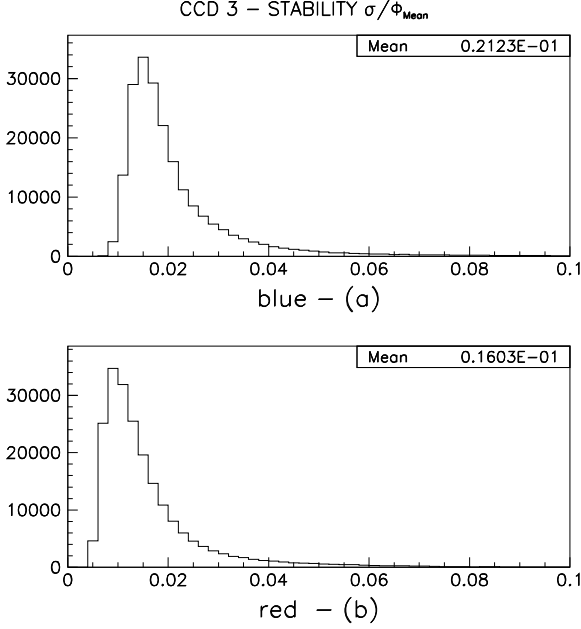


Fig. 11. Flux stability achieved on *super-pixel* light curves in blue (a) and in red (b) for all the pixels of CCD 3 (before the seeing correction)

a large part using the fact that the flux of each super-pixel is correlated in a specific way with the seeing value.

5.1. Correlation between flux and seeing

Depending on their position with respect to the nearest star, super-pixel fluxes can significantly anti-correlate with the seeing if the super-pixel is in the seeing spot, or correlate if it lies in the tail of a star. A correlation coefficient for each super-pixel p can be computed using the usual formula:

$$\rho^p = \frac{\sum_n (\phi_n^p - \langle \phi \rangle) (S_n - \langle S \rangle)}{\sqrt{\sum_n (\phi_n^p - \langle \phi \rangle)^2 \sum_n (S_n - \langle S \rangle)^2}} \quad (6)$$

where $\langle \phi \rangle$ and $\langle S \rangle$ are the mean values of the super-pixel flux ϕ_n^p and seeing S_n on night n . On the upper panels of Fig. 12, we show the distributions of correlation coefficients ρ^p in blue (left) and in red (right) for each super-pixel p . These histograms look quite different in both color but both distributions have a peak around $\rho \simeq -0.8$. This peak, which corresponds to the anti-correlation with seeing near the center of resolved stars, is expected due to the large number of resolved stars. It is higher in red than in blue, which is consistent with the EROS color-magnitude diagram where most detected stars have $B - R > 0$ (Renault et al. 1996). The correlation with seeing expected for star tails ($\rho > 0$) is not seen as clearly. However, a clear excess at high value of ρ (around $\rho \simeq 0.6$) appears in red, again consistent with the EROS color-magnitude diagram.

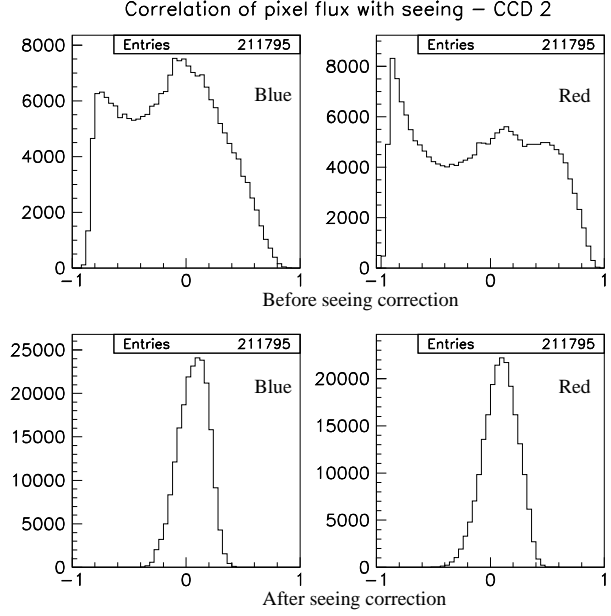


Fig. 12. Histogram of the correlation coefficient ρ between the super-pixel flux and the seeing.

Figure 13 gives an example of such a correlation. The upper left panel of Fig. 13 displays the scatter diagram of one super-pixel flux versus the seeing, corresponding to a correlation coefficient $\rho^p = -0.95$. The bottom left panel displays the light curve of this super-pixel. Despite the intrinsic dispersion of the measurements (which could be large especially when a temporal variation occurs), a linear relationship is observed.

5.2. Correction

The idea is to correct this behaviour using the following linear correction:

$$\phi_n^p|_{\text{corrected}} = \phi_n^p - a^p (S_n - \langle S \rangle) \quad (7)$$

where a^p is the estimate of the slope for each super-pixel and $\phi_n^p|_{\text{corrected}}$ is the corrected flux, used in the following.

The effect of this correction is illustrated on the right panels of Fig. 13. The upper right panel shows the scatter diagram after the correction, whereas the right bottom panel displays the corrected light curve.

As shown on the bottom panels of Fig. 12, this correction removes any significant correlation with the seeing. The efficacy of this approach is due to the very good sampling of these data: the seeing of the averaged images is randomly distributed as a function of time and cannot produce the kind of intrinsic variations we are looking for. Accordingly, we do not expect this correction, designed to reduce the noise due to the seeing variations, to destroy possible variations.

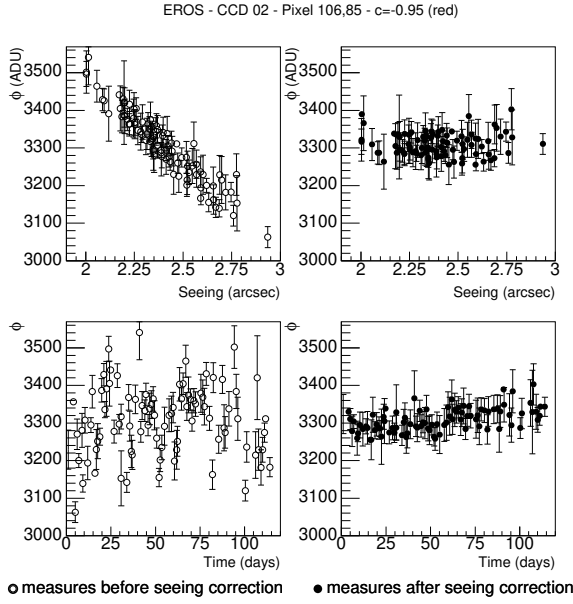


Fig. 13. Seeing correction applied on the flux of one super-pixel light curve anti-correlated with the seeing ($\rho^p = -0.95$). See text for further details.

Finally, this linear correction can only correct for first order effects. Its success stems from the fact that the seeing dispersion has been significantly reduced through the averaging procedure.

5.3. Stability after the seeing correction

The correction described above significantly reduces the fluctuations due to the seeing variations. Figure 14 displays the relative dispersion computed after this correction. With respect to the histograms presented in Fig. 11, this dispersion is reduced by 20% in blue and 10% in red, achieving a stability of 1.8% in blue and 1.3% in red. Small fluctuations are observed between the CCD fields.

This stability can be expressed in term of detectable change in magnitude: taking into account a typical seeing fraction of 80% for a super-pixel, and assuming a total background characterized by a surface magnitude $\mu_B \simeq 20$ in blue and $\mu_R \simeq 19$ in red, stars variations will be detected 5σ above the noise if the star magnitude gets brighter than 20 in blue and 19 in red at maximum. With the Pixel Method, the detectability of a variation is not hindered by star crowding as we do not require to resolve the star.

6. Error estimates

This section is dedicated to the evaluation of the errors which remain after the data treatment presented above. We first describe the noise and systematic effects that we

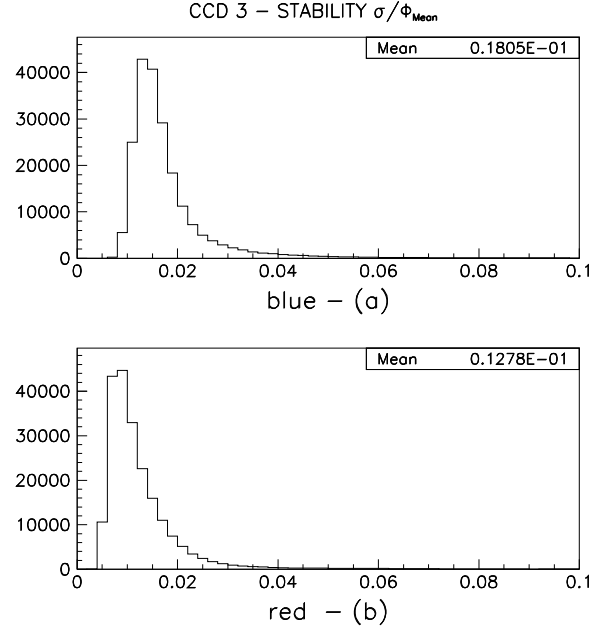


Fig. 14. Flux stability achieved on *super-pixel* light curves after seeing correction in blue (a) and in red (b), for all the pixels of CCD 3.

intend to include in error bars. Secondly, we compute error estimates on the flux of each super-pixel. Thirdly, we compare these error estimates computed on real light curves with simulations, based on the understanding of these errors. These error estimates are crucial for the trigger described in Paper II.

6.1. Motivations

The relative dispersions presented in Fig. 14 give an overview of the level of noise affecting super-pixel flux measurements. However, the statistical fluctuations, which could easily be estimated, are not a dominant source of noise. The aim of this section is the construction of an error bar for each super-pixel measurement.

Residual systematic effects A visual inspection of light curves shows residual systematic effects, mainly affecting measurements on particular nights. We are not able to correct these systematic effects, and are conscious that part of them are probably due to the following points.

The seeing correction is empirical and the linearity is certainly of first order. It can be sensitive to bad seeing determination due to inhomogeneous seeing across the image or (slightly) elongated PSF. Part of these problems are certainly due to atmospheric dispersion as mentioned by Tomaney & Crotts (1996). This phenomenon depends on wavelength, correlates with air mass, and affects differently stars with different color. This is a serious problem

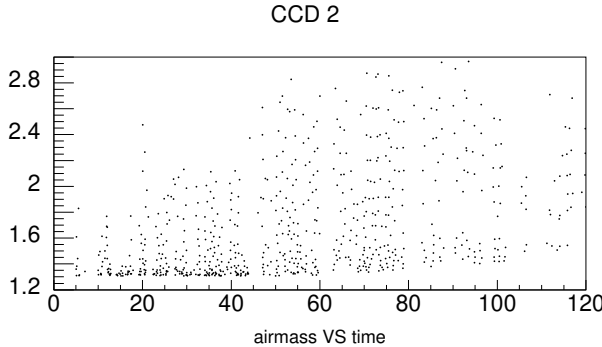


Fig. 15. Air masses towards the LMC for each individual images.

for pixel monitoring as we do not know the color of unresolved stars. Figure 15 displays the air mass towards the LMC as a function of time for the images studied (before the averaging procedure), and shows a quite large dispersion of air mass during the night. All the measurements have an air mass larger than 1.3, and moreover half of them have an air mass larger than 1.6, producing non negligible atmospheric prism effects because of the large pass-band of the filters; according to Filippenko (1982), photons at the wavelength extremes of our filters are spread over 0.73 to 2.75 arcsecond in blue depending on the air mass, and over 0.34 to 1.17 arcsecond in red.

Furthermore, some systematic effects can also come from the alignments, in particular the geometric one as discussed above.

We expect all these problems to be considerably reduced by the averaging procedure. However, due to varying observing conditions each night is different. For instance the seeing distribution over one night can differ from the global one. This can introduce systematic effects very difficult to keep track of and to correct. Nevertheless, as these residual effects concern isolated points of some light curves, it is possible to include them into the error bars, with a “quality factor” computed for each image as described in the next section.

6.2. Taking noise into account

As explained in previous sections, it is not straightforward to trace the errors affecting pixel fluxes through the various corrections. Errors are estimated here in a global way for each pixel flux, “global” meaning that we do not separate the various sources of noise. The images used for the averaging procedure provide a first estimate of these errors. The dispersion of the flux measurements performed over each night allows the computation of an error associated with the mean value. We discuss how this estimate deviates from gaussian behaviour, and which correction can be applied. Gaussian behaviour is of course an ideal

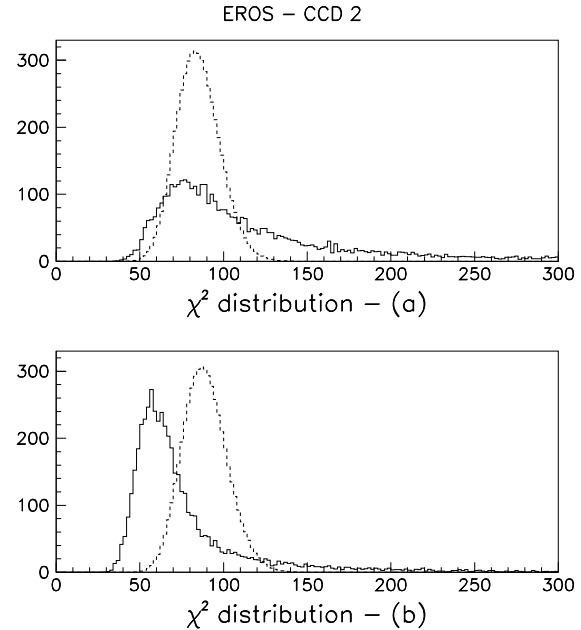


Fig. 16. Distributions of χ^2 : on both panels, the dashed line represents the ideal distribution discussed in the text. Figure (a) (solid line) displays the χ^2 distributions with error estimates based on the dispersion of pixel measurements over each night. In figure (b), the histogram (solid line) is computed with errors calculated for each pixel flux as the maximum between the photon noise and the errors used in figure (a).

case, but it gives a reference for the different estimates discussed here.

Error estimates on elementary pixel When we perform for each night n the averaging of pixel fluxes, we also measure a standard deviation for each pixel $\sigma_{\phi_n^p}$. Assuming this dispersion is a good estimate of the error associated to each flux measurement $\phi_{n,j}^p$, then supposing errors affecting each measurements are independent, we can deduce an error σ_n^p on ϕ_n^p as:

$$\sigma_n^p = \frac{1}{N_n^p} \sigma_{\phi_n^p}^2 \quad (8)$$

This estimation, however, is itself uncertain: the number of images per night can be quite small, and Eq. (8) assumes identical weight for all images of the night. Moreover, as already said, Eq. (8) does not take into account systematic effects which change from night to night.

In order to qualify our error estimates, we compute the distribution of the χ^p values associated with each pixel p light curve.

$$\chi^p = \sum_n \frac{(\phi_n^p - \langle \phi^p \rangle)^2}{\sigma_n^p} \quad (9)$$

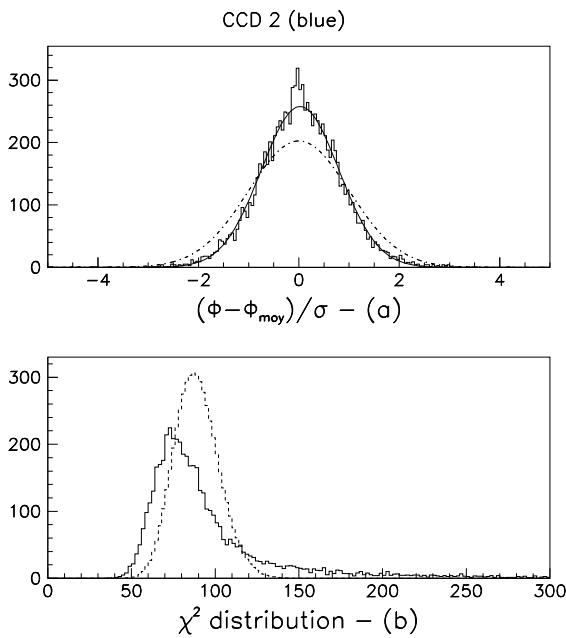


Fig. 17. Corrected error bars: the upper panel (a) displays a z_n distribution for a given image n whose errors were over-estimated (histogram). The full line corresponds to the fitted gaussian distribution, and the dashed line to the normalized gaussian distribution. The lower panel (b) shows the χ^2 distribution calculated with the corrected errors (solid line).

Figure 16-a displays two χ^2 distributions: the ideal case (dashed line) assumes gaussian noise and the number of degree of freedom³ (hereafter NDOF) of the data; the solid line uses real data with errors computed with Eq. (8): the histogram peaks roughly to the correct NDOF, but exhibits an important tail corresponding to non-gaussian and under-estimated errors.

Due to statistical uncertainties on the calculation of the errors, it happens that some of them are found smaller than the corresponding photon noise. The maximum of the calculated error and the photon noise is then associated to each measurement and called σ_n^p in the following. The corresponding χ^2 distribution displayed (solid line) in Fig. 16-b has a smaller non-gaussian tail, but peaks at a smaller NDOF: not surprisingly the errors are now over-estimated.

Correction The correction described here is intended to account for night to night variations, or important system-

³ Note that with this procedure 3 points do not have error bars because only one image is available during the corresponding night. As discussed below, an error will be associated with these points in the following, and this explained why the gaussian distribution of Fig. 16-a (dashed line) is slightly shifted towards the left with respect to those in Fig. 16-b and Fig. 17-b.

atic effects altering some images. We will weight each error with a coefficient depending on the composite image. The principle is to consider the z_n distribution for each night n of the variable z_n^p given by:

$$z_n^p = \frac{\phi_n^p - \langle \phi^p \rangle_n}{\sigma_n^p} \quad (10)$$

and to renormalize it in order to obtain a normal gaussian distribution. $\langle \phi^p \rangle_n$ is the mean pixel p flux value computed over the whole light curve. The standard deviation σ'_n of these z_n distributions is estimated for each mean image n on a central patch⁴ of 100×100 pixels. Such z_n distributions are plotted for each image n and a gaussian distribution is fitted to the data. This fit is quite good for most of the images and the dispersion of the gaussian distribution is our estimate of σ'_n . Figure 17-a shows an example of the σ'_n estimation. The solid line shows the fit of a gaussian to the data. The width is not equal to 1 as it should, but to 0.77, the value of σ'_n for this image. For comparison, we show a gaussian of width 1, with the same normalization (dashed line).

In the following, the corrected errors:

$$\sigma_n^p|_{\text{corrected}} = \sigma'_n \sigma_n^p \quad (11)$$

are associated with each pixel flux. σ_n^p is different for each measurement whereas σ'_n is a constant for each image n . The resulting χ^2 histogram is displayed in Fig. 17-b (full line). The χ^2 distribution peaks at a higher value of χ^2 than before correction (Fig. 16-b), which however is still slightly smaller than the NDOF.

From pixel errors to super-pixel errors We have seen in Sect. 4.2 that the use of super-pixel light curves allows to reduce significantly the flux dispersion along the light curves. The most natural approximation for the computation of super-pixel errors is to assume those on elementary pixels to be independent:

$$\sigma_n^{sp} = \sqrt{\sum_p \sigma_n^p} \quad (12)$$

We then account for this approximation by the correction discussed above, now performed on super-pixel light curves. The coefficients $\sigma'_n|_{sp}$ are 20% larger than the previous ones, showing that pixel errors are not really independent.

We have now super-pixel light curves with an error estimate for each flux. Figure 18 displays an example of a typical stable light curve in blue (upper panel) and in red (lower panel). The flux in ADU is plotted as a function of time in days. (Day zero is JD 2448608.5.)

⁴ The values of this dispersion σ'_n fluctuate around 4% from patch to patch.

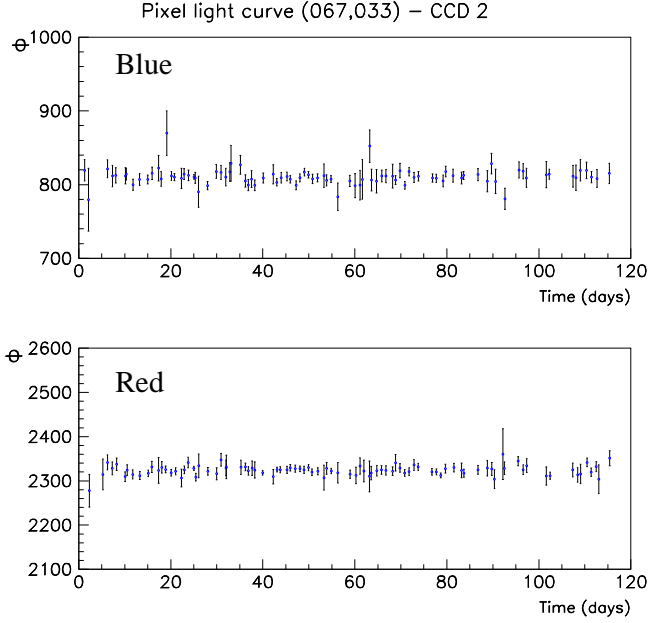


Fig. 18. Example of a stable super-pixel light curves

6.3. Modeling the noise

The idea is to reproduce with simulations the main features of the light curves, and in particular the noise. This is useful for the estimation of the number of microlensing events which can be expected with this data set, as well as for the computation of the detection efficiencies (in Paper II).

We simulate stable super-pixel light curves, “stable” meaning free of any microlensing events or variable stars. We use the characteristics of the raw data. First, we adjust the background flux (sky and galaxy) with the mean flux measured on our reference images. Then according to a luminosity function (see Baillon et al., 1993), the flux of a single star, for which seeing variations are taken into account, is added. The star flux is computed assuming black body spectra. Various efficiencies characterizing the detector are taken into account (CCD, filters, mirrors...).

We calculate the photon noise affecting the super-pixel flux according to the variations of the background flux and the absorption factor. Read-out noise is also added. We compute the mean super-pixel flux for each simulated “night”. Then, we perform the noise estimates as described in Sect. 6.2, except that we do not put in correction factors (σ') accounting for night to night variations. One these simulated curves, we do not take into account errors from the alignments and seeing variations due to surrounding stars.

Comparison of simulations with data In order to match the real χ^2 distribution computed along the super-pixel light curve, we find that errors for simulated light curves need

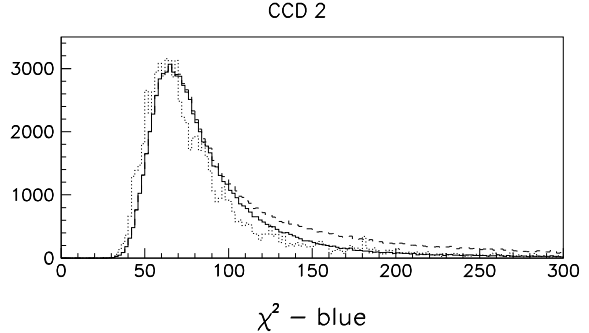


Fig. 19. Distributions of χ^2 : The full and dashed lines represent the measured distributions in the blue band; the full line corresponds to light curves with no bump (see text), the dashed line corresponds to all super-pixel. The dotted one represents the χ^2 distribution measured on simulated light curves.

to be multiplied by a factor 1.4 in both colors. This was expected given our simplifications. However this remains in the range of the values computed for σ' : depending on the CCD field, the mean σ' lies between 1 and 1.5. Figure 19 displays the χ^2 distribution associated with these simulated light curves (dotted line) superimposed on real ones (full and dashed lines): the dashed line presents the histogram for all the super-pixels of one CCD field: the tail at high value is larger than for simulations; the solid line corresponds to “non-variable” super-pixels⁵. The upper tail is significantly reduced.

The simulated distribution matches the real one quite well: the main features of the histograms are reproduced. This shows that errors computed for the simulations are reasonable and the efficacy of the operations applied to the data. This also demonstrates that real light curves are not affected by a high level of unexpected noise.

7. Conclusion

The treatment described here produces super-pixel light curves with a level of noise compatible with the expectations of Baillon et al. (1993): dispersions of 1.8% of the flux in blue and 1.3% in red are measured over a 120 days time period. Variations of the observational conditions have been successfully corrected. Noises have been considerably reduced thanks to the averaging of the images of each night. This turns out to be a crucial step as it has allowed to reduce the effects of the dispersion of the observational conditions. Moreover, the fluctuations due to seeing variations have been greatly reduced. We have shown that we understand the super-pixel light curves obtained, and that no significant unexpected source of noise affects the measurements.

⁵ We keep the light curves with no bump, defined as 3 consecutive points above a base flux by more than $3 \times \sigma$.

The careful estimates of error bars performed in Sect. 6 will be an important ingredient for the microlensing Monte-Carlo simulations described in Paper II, as first emphasized by Baillon et al. (1993) whose results relied on crude error estimates. With selection criteria similar to those used in Baillon et al. (1993), simulations including realistic error estimates give the following results (comparable with the preliminary Baillon et al. result): if one considers that a fraction f of the galactic halo is filled with $0.1 - 0.5 M_{\odot}$ compact objects, about $1. \times f$ microlensing events are expected with the light curves obtained. This will be further discussed in Paper II, where a complete analysis of these pixel light curves will be described.

Acknowledgements. We thank A. Gould for extremely useful discussions and suggestions. We are also particularly grateful to Claude Lamy for her useful help on data handling during this work. P. Gondolo was partially supported by the European Community (EC contract no. CHRX-CT93-0120). A.L. Melchior has been supported by grants from the Singer-Polignac Foundation, the British Council, the DOE and by NASA grant NAG5-2788 at Fermilab.

References

Alard, C., et al.: 1995, *ESO Messenger*, **80**, 31

Alcock, C., et al.: 1996, *ApJ, astro-ph/9606165* **00**, 00

Alcock, C., et al., W.: 1995, *ApJ* **445**, 133

Alcock, C., et al.: 1993, *Nat* **365**, 621

Ansari, R.: 1994, *Une méthode de reconstruction photométrique pour l'expérience EROS*, preprint LAL 94-10

Ansari, R., et al., G.: 1997, *A&A* **324**, 843

Arnaud, M. et al.: 1994a, *Experimental astronomy* **4**, 279

Arnaud, M. et al.: 1994b, *Experimental astronomy* **4**, 279

Ashman, K. M.: 1992, *PASP* **104**, 682

Aubourg, E., et al.: 1993, *Nat* **365**, 623

Aubourg, E., et al.: 1995, *A&A* **301**, 1A

Baillon, P., et al.: 1993, *A&A* **277**, 1

Carollo, C. M., et al.: 1995, *ApJ* **441**, L25

Carr, B.: 1994, *ARA&A* **32**, 531

Copi, C. J., et al.: 1995, *Sci* **267**, 192

Crotts, A. P. S.: 1992, *ApJ* **399**, L43

Evans, N. W.: 1994, *ApJ* **437**, L31

Filippenko, A. V.: 1982, *PASP* **94**, 715

Gerhard, O. and Silk, J.: 1996, *ApJ* **472**, 34

Giraud-Héraud, Y.: 1997, *AGAPE, Andromeda Gravitational And Pixel Experiment*, 3rd Microlensing Workshop, Notre-Dame, USA

Gould, A.: 1995, *ApJ* **455**, 44G

Gould, A.: 1996a, in *Sheffield workshop on Identification of Dark Matter - astro-ph/9611185*

Gould, A.: 1996b, *ApJ* **470**, 201

Grison, P.: 1994, *Ph.D. thesis*, Université de Paris VII, Paris

Grison, P., et al.: 1995, *A&AS* **109**, 447

Kerins, E. J.: 1997, *A&A* **322**, 709

Paczynski, B.: 1986, *ApJ* **304**, 1

Persic, M. and Salucci, P.: 1992, *MNRAS* **258**, 14P

Queinnec, F.: 1994, *Ph.D. thesis*, Université de Paris VII, Paris

Renault, C.: 1996, *Ph.D. thesis*, Université de Paris VII, Paris

Stanek, K. Z. et al.: 1997, *ApJ* **477**, 163

Tomaney, A. B. and Crotts, A.: 1996, *AJ* **112**, 2872

Udalski, A., et al.: 1995, *Acta Astron.* **45**, 237

Walker, T. P., et al.: 1991, *ApJ* **376**, 51

White, M., et al.: 1996, *MNRAS* **283**, 107

Zaritsky, D.: 1992, *PASP* **104**, 831